Journal of Magnetic Resonance 299 (2019) 196–201

Contents lists available at ScienceDirect

Journal of Magnetic Resonance

journal homepage: www.elsevier.com/locate/jmr

Microscale 3D imaging by magnetic resonance force microscopy using full-volume Fourier- and Hadamard-encoding

Sebastian Schnoz [a], Andreas Hunkeler [a], Alexander Däpp [a], Robert Kamberger [b], Jan G. Korvink [c], Beat H. Meier [a,*]

[a] Physical Chemistry, ETH Zurich, Vladimir-Prelog-Weg 2, 8093 Zurich, Switzerland
[b] BrainLinks-BrainTools Cluster of Excellence, University of Freiburg, Georges-Koehler-Allee 80, 79110 Freiburg, Germany
[c] Institute of Microstructure Technology, KIT, Hermann-von-Helmholtz-Platz 1, 76344 Eggenstein-Leopoldshafen, Germany

ARTICLE INFO

Article history:
Received 23 October 2018
Revised 9 January 2019
Accepted 10 January 2019
Available online 14 January 2019

Keywords:
Magnetic-resonance force detection
MRFM
Micro MRI

ABSTRACT

Three-dimensional spatially resolved full-volume imaging by magnetic resonance force microscopy at room temperature is described. Spatial resolution in z-dimension is achieved by using the magnetic-field gradient of a ferromagnetic particle that is also used for the force detection of the magnetic resonance. The gradient of the radiofrequency pulses generated by two separate wire-bonded microcoils is used for spatial resolution in x- and y-dimension. To enhance the sensitivity of our measurement Hadamard- and Fourier-encoding schemes are applied due to their multiplex effect. Measurements were taken on a patterned $(NH_4)_2SO_4$ crystal sample. From the calculated magnetic field distributions, a 3D image was reconstructed with a voxel volume of about 5 μm^3 (1.2 $\mu m \times 3.0\ \mu m \times 1.4\ \mu m$ in x-, y- and z-dimension).

© 2019 Elsevier Inc. All rights reserved.

1. Introduction

Magnetic resonance imaging (MRI) is a versatile, well-developed and noninvasive method to image and investigate different samples ranging from materials to humans. Its chemical selectivity and the possibility to add different contrast methods (e.g., T_1 and T_2 contrast, chemical shifts, diffusion, paramagnetic relaxation) allow the combination of various sample properties, or spectroscopic dimensions, with spatially resolved imaging.

The current limit of resolution for liquid samples is a few micrometers for MRI microscopy with the best achieved resolution up to now of $3 \times 3 \times 3\ \mu m$ at a static magnetic field of 18.8 T [1]. For solid samples with a broader NMR linewidth the resolution is lower at $8 \times 8 \times 8\ \mu m$ [2,3] at room temperature and $2.8 \times 2.8 \times 2.8\ \mu m$ at 28 K [4].

The reasons for these limitations are the rather low sensitivity of inductively detected NMR and the difficulty to further increase the magnetic field gradients above the value of 65 T/m used by Weiger et al. To overcome these limitations alternative approaches must be investigated. A promising method is magnetic resonance force microscopy (MRFM). It uses a micromechanical resonator (cantilever) acting as a magnetometer. This force sensor is used to detect the presence of spin magnetization. In the sample-on-cantilever geometry the sample of interest is attached to the tip of the cantilever and placed in an external magnetic field B_{ext}. The force on the cantilever has its origin in the interaction of the sample's spin magnetization with an inhomogeneous magnetic field produced by a nearby ferromagnetic particle [5–9]. The sign of this force is changed by inverting the spin magnetization periodically at the cantilever's resonance frequency by an adiabatic fast passage rf pulse. This results in a driven damped oscillation of the cantilever whose amplitude can be measured by laser-beam deflection. For small samples and detectors (micrometers and less) it could be shown that force detection of magnetic resonance becomes more sensitive than inductive detection [10]. Furthermore, producing a magnetic field gradient by a micron-sized ferromagnetic particle allows for very strong gradients up to 4 million T/m and therefore higher resolution compared to magnetic field gradients produced by coils [11].

Züger et al. presented first three-dimensional imaging with MRFM using a scanning-probe technique at room temperature resulting in a resolution of 3.6 μm [12]. Other groups reported similar measurements [13,14]. Pushing the resolution down to the low nanometer range requires the lowering of the temperature to reduce the thermal noise of the cantilever motion. Mamin et al. achieved a resolution of $90 \times 90 \times 80$ nm at cryogenic temperature [15] which was further improved by Degen et al. with a resolution

* Corresponding author.
E-mail address: beme@ethz.ch (B.H. Meier).

https://doi.org/10.1016/j.jmr.2019.01.005
1090-7807/© 2019 Elsevier Inc. All rights reserved.

of about 4 nm in the x-direction and between 4 and 10 nm in the other directions [11].

2D spatially resolved MRFM-imaging at room temperature using a Hadamard- and Fourier-encoding scheme was demonstrated [16] at a mean resolution of 1 × 1 μm while keeping the position of the sample, gradient and detector constant. Here we present the extension of this method to 3D spatially resolved imaging. The spin signal is spatially resolved in the z-dimension by the gradient produced by a nearby ferromagnetic particle. Wire-bonded microcoils are used to produce rf-gradients in the x- and y-dimension (Fig. 1).

2. Results

To show that our method can resolve features we used a test sample consisting of a $(NH_4)_2SO_4$ single crystal shaped to the letters "ETH" by focused ion beam milling. Dimensions of the sample were 43 μm × 70 μm × 23 μm in x-, y- and z-dimension. The sample was glued to the tip of a cantilever and mounted into the setup as shown in Fig. 2. We measured the signal from the ^{1}H spins of the sample.

The pulse sequence for a 3D imaging experiment is given in Fig. 3. In the x- and y-dimensions Fourier-encoding is applied performing a nutation experiment in the presence of an rf gradient. Spins further away from the x-coil will nutate slower around the x-axis under an rf pulse. A nutation curve is recorded by increasing the nutation-time step by step (leaving the pulse amplitude constant). Fourier transformation of the nutation curve results in the distribution of nutation frequencies along the x-axis. Knowing the gradient of the field B_1 along the x-dimension allows to calculate a spatial axis from the nutation axis. The scheme was applied for the y-dimension. During x- and y-encoding the cylindrical B_0 gradient source was flipped away from the sample to minimize the field inhomogeneity and reduce off-resonance effects during the nutation pulses (see Fig. 3) [16]. A waiting time of 1 ms between the x- and the y-pulse destroys the remaining transverse magnetization (z-filter). Before encoding of the spins along the z-axis and acquisition, the gradient source was flipped back within 200 ms after which the transverse magnetization is decayed. Spatial encoding of the remaining longitudinal spin magnetization in the z-dimension is done by the B_0 gradient along the z-dimension produced by a nearby cylindrically shaped ferromagnet. The presence of this gradient allows to select a resonance slice for detection by adjusting the carrier frequency and the width of the adiabatic inversion pulse during detection (generated by the x-coil). Stepping the resonance slice through the sample leads to an image along the z-dimension. Instead of slice-by-slice detection we used Hadamard-encoding [17]. Note that the spatial encoding and image reconstruction for every spatial dimension can be done independently if the gradients are aligned orthogonally to each other.

The 3D-MRFM image of the test sample is shown in Fig. 4(a). The letter "T" and "H" are clearly visible and well resolved. The letter "E" is only visible towards the top. The most likely reason might be a lower rf amplitude for locations further away from the x-coil which could be the case for the lower part of the "E" due to the slightly tilted positioning of the sample on the cantilever. This leads to signal loss during detection since the inversion sweeps are not adiabatic for low rf powers.

Fig. 5(a) shows an image slice perpendicular to the z-axis located at about 213 μm from the gradient source. The lower part of the letter "T" and "H" are well resolved over the entire sample dimension along the y-axis. Fig. 5(b) shows an image slice perpendicular to the y-axis located at a distance of about 50 μm from the y-coil. The slice is well resolved except the lower part of the letter "E".

Due to the non-linearity of the gradient of the magnetic fields, the voxel size in the imaged volume varies from 1 μm to 1.6 μm along the x-direction, from 2.2 μm to 6.9 μm along the y-direction and from 1.2 μm to 1.5 μm along the z-direction (calculated using the equations given in the Setup Section). The mean voxel dimensions of our experiment are about 1.2 μm in x-direction, 3.0 μm in y-direction and 1.4 μm in z-direction. Consequently, we have imaged voxels with a mean size of about 5 μm^3. The smallest voxel contains about 1.7×10^{11} spins corresponding to a net Boltzmann polarization of about 4.6×10^5 fully polarized spins.

The resolution in the images cannot exceed the voxel size, but it can be lower caused by linewidth, pulse imperfections or drift. We therefore compare a 2D slice from the measured image (Fig. 6(a)) with 2D simulated images in the xz-plane where the sample features are best resolved. For Fig. 6(b) to (d) an image with a voxel size of 1 μm × 1 μm, slightly smaller than our experimental voxel size, was produced. A Gaussian blur was then applied with the standard deviation $\sigma \approx 0.88$ μm, 1.24 μm and 1.59 μm, for (b), (c) and (d), respectively. According to the Sparrow criterion for distinguishing two points in an image [18], the resolution ρ of such a Gaussian blur is given by $\rho = \sqrt{2}\,\sigma$ which corresponds to a resolution along the x- and z-axis of 1.25 μm, 1.75 μm and 2.25 μm, respectively. Optical inspection of the measured and simulated images shows best agreement for a resolution of 1.75 μm along the x- and z-dimension. We didn't take the cursive feature of the

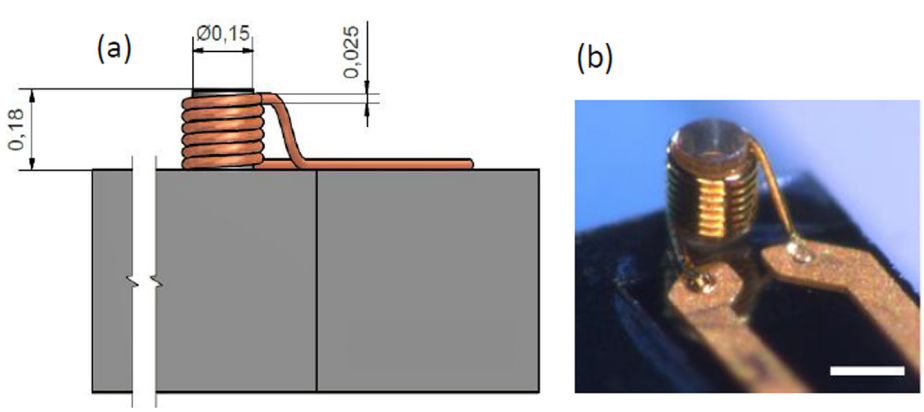

Fig. 1. Microcoils for encoding the x- and y-dimension. The microcoils are wire-bonded and made of gold. There are 6 windings wound around a SU-8 post (epoxy-based photoresist). The endings of the coil are attached to gold pads on a glass or silicon chip. The gold pads were contacted by copper cables and the whole coil was integrated into a LRC-circuit. (a) Shows the dimensions of the coil in a schematic drawing (dimensions in mm). (b) Shows a photograph of a microcoil. The scale bar is 150 μm.

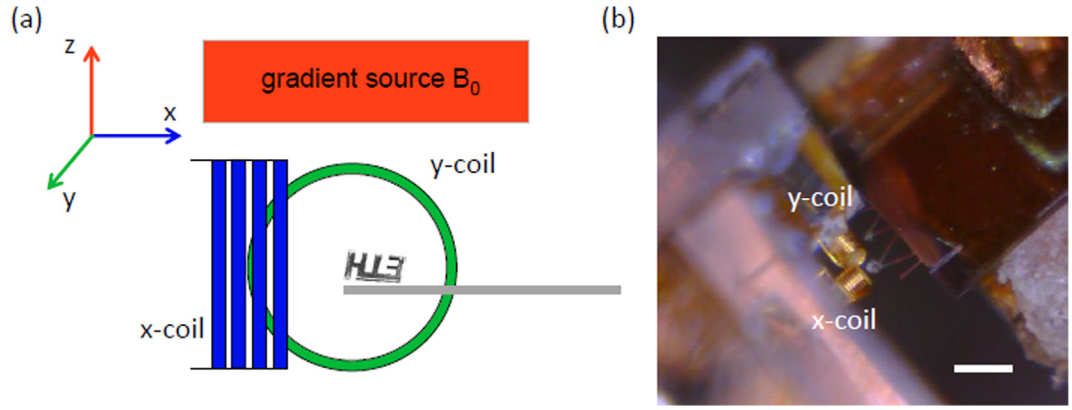

Fig. 2. (a) The schematic setup of the experiment is shown. The static magnetic field B_0 along the z-axis is produces by a cylindrically shaped iron-cobalt alloy. The rf fields along the x- and y-axis (B_1 and B_2) are generated by two wire-bonded microcoils. Within the limits of alignment, the two coils and the gradient are mutually orthogonal to each other. The proportion of the sample size and the diameter of the coils and gradient are at scale. (b) Photograph of the (triangular) cantilever with sample attached to the tip and the coils. The cylindrical gradient source isn't shown. The scale bar is 500 μm.

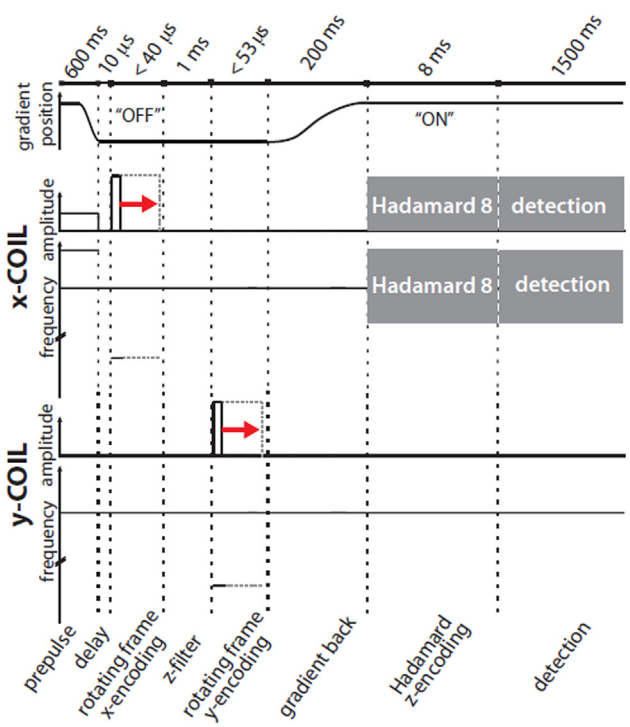

Fig. 3. The pulse sequence of the 3D-imaging experiment is shown. First, the cylindrical gradient source is flipped away from the sample. During this time a prepulse is applied to preheat the cantilever and reduce rf-cantilever interactions. A nutation pulse is applied by the x-coil to encode the signal along the x-dimension. A z-filter makes sure the remaining transverse magnetization is decayed before the nutation pulse of the y-coil encodes the y-dimension. The gradient source is flipped back over the sample and the magnetization is encoded along the z-axis by Hadamard-encoding. Finally, the signal is detected by adiabatic inversion pulses.

ETH-logo into account which leaves our conclusions unaltered. For resolution along the y-axis where the voxel size is 3 μm we assume, by analogy, a resolution of 3.5 μm.

3. Methods

3.1. Setup

All measurements were done on a home-built MRFM setup [19,20] at room temperature and a pressure of lower than 10^{-3} mbar in a magnetic field B_{ext} of 5.87 T (250 MHz Larmor frequency). We used a commercially available cantilever (Veeco Instruments, MLCT-NOHW) with a quality factor $Q \sim 3000$ in the vacuum environment of the experiment. The cantilever oscillates parallel to the field B_{ext} and is operated in amplitude-detection mode [7,8,21]. The gradient of the magnetic field B_0 along the z-dimension was produced by a cylindrically shaped iron-cobalt alloy (B_{sat} = 2.3 T, radius $R \sim 100$ μm, length $L \sim 3$ mm). On the symmetry axis (z-axis) of the cylinder and assuming the length L of the cylinder being much bigger than its radius R, the magnetic field can be approximated by

$$B_{0,z}(z) = \frac{B_{sat}}{2}\left(1 - \frac{z}{\sqrt{z^2 + R^2}}\right) \quad (1)$$

The cylindrical gradient source is attached to a piezo bender actuator (Physikinstrumente, Germany) to flip the gradient source 1 mm away from the sample during encoding with B_1 and B_2 to reduce the B_0 gradient and avoid off-resonance effects.

The magnetic fields B_1 and B_2 in the x- and y-dimension are generated by wire-bonded microcoils. The microcoils consist of 6 windings made of a 25 μm diameter gold wire, have a length of about 180 μm and an inner diameter of 150 μm. The coils are wound around a cylindrical SU-8 post attached to a glass chip (Fig. 1). On the symmetry axis of the coil (x-/y-axis) and assuming its length being much bigger than its diameter the magnetic field) and its gradient = can be approximated by

$$B_{1,x}(x) = \frac{\mu_0 In}{2}\left(1 - \frac{x}{\sqrt{x^2 + R^2}}\right) \quad (2)$$

with I the current through the coil, n the number of windings per length of coil and μ_0 the magnetic constant. Note that the formula in Eq. (2) holds for the x- and the y-coil. Additionally to generating the field gradient along the x-dimension, the x-coil is also used for the adiabatic inversion sweeps during the detection period. Fig. 7 shows simulations of the magnetic fields produced by the ferromagnetic cylinder and the coils. Simulations were made with Computer Simulation Technology software (CST). The average magnitude of the imaging gradients at the sample's position is 235 T/m in x-direction, 62 T/m in y-direction and 878 T/m in z-direction.

The wire-bonded microcoils are wound from thinner wire compared to the hand-made microcoils (wire diameter ~60 μm) used in earlier work [16]. This allows for more windings per length which should increase the gradient strength when the current

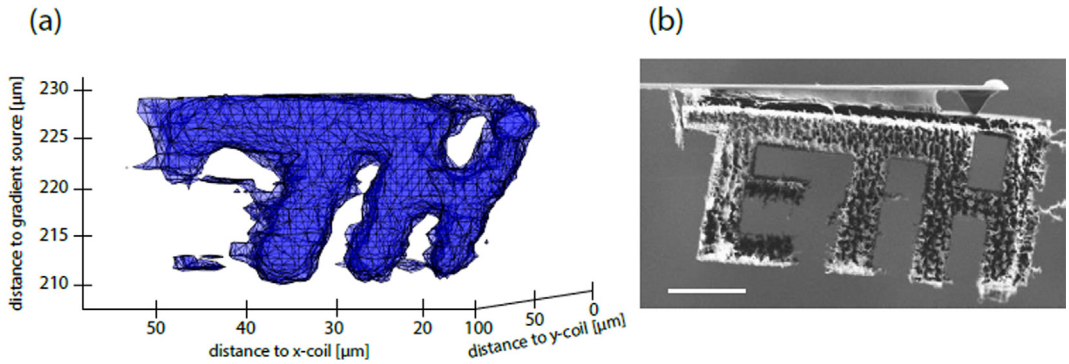

Fig. 4. (a) A 3D image by MRFM is shown. The image is partially resolved and the letters "T" and "H" are clearly visible. The letter "E" is present only rudimentarily. This is most likely caused by the lower rf field amplitude during detection for sample parts further away from the x-coil resulting in signal loss. (b) SEM image of the sample glued to the tip of a cantilever is shown. The scale bar is about 10 µm.

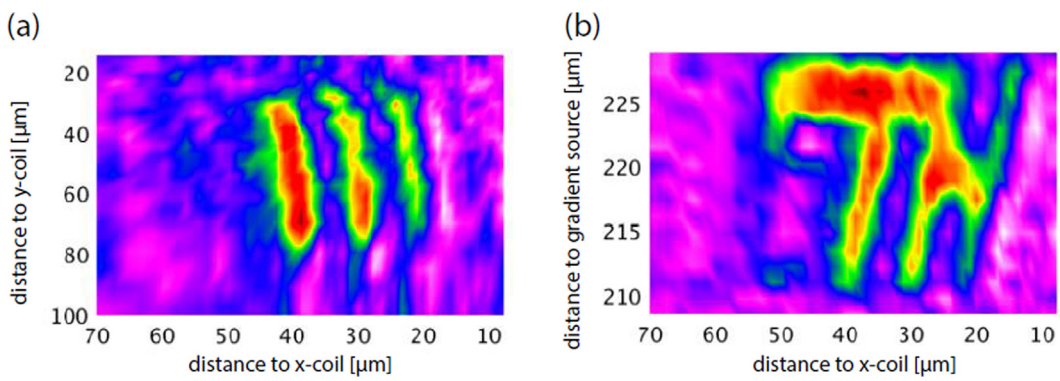

Fig. 5. Image slice along the z-axis (a) and the y-axis (b) of the 3D-MRFM image in Fig. 4(a) are shown. The slice along the z-axis is located at a distance of about 213 µm from the cylindrical gradient source. The slice along the y-axis is located at a distance of about 50 µm from the y-coil. The structure of the sample is partially resolved.

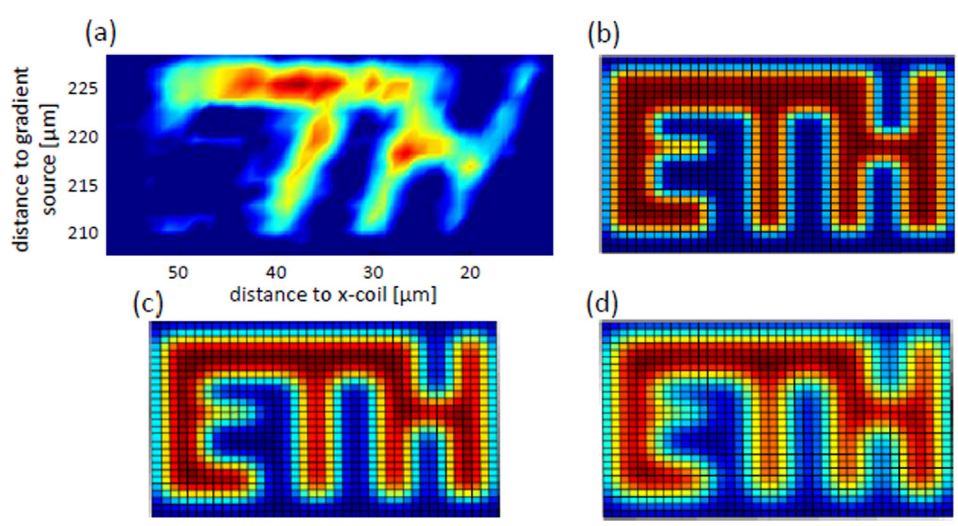

Fig. 6. (a) 2D slice from 3D image of the ETH-logo perpendicular to the y-axis located in the center of the sample. (b)-(d) Simulated 2D images of a slice perpendicular to the y-axis. A Gaussian blur in 2D was applied with $\sigma \approx 0.88$ µm, 1.24 µm and 1.59 µm, respectively, for the x- and z-dimension leading to an effective voxel size of (b)1.25 µm, (c) 1.75 µm and (d) 2.25 µm.

density is kept constant. In our experiment the wire-bonded microcoils showed only a slightly higher gradient strength compared to the hand-made coils. The reason was the lower current density we sent through the coils since thinner wires are supposed to support less current density (due to heating effects) and we didn't want to risk destroying the coils before the measurements were finished. We assume that higher current densities are possible since the construction of the coils allows for a more efficient transport of the generated heat away from the coils compared to the hand-made coils. The wire-bonded coils are wound around a SU-8 post, are close to a glass chip and the endings of the thin wire of gold are kept short and are connected to gold pads. This allows for a more efficient transport of the heat away from the coil compared to the free hanging hand-made coils in the vacuum

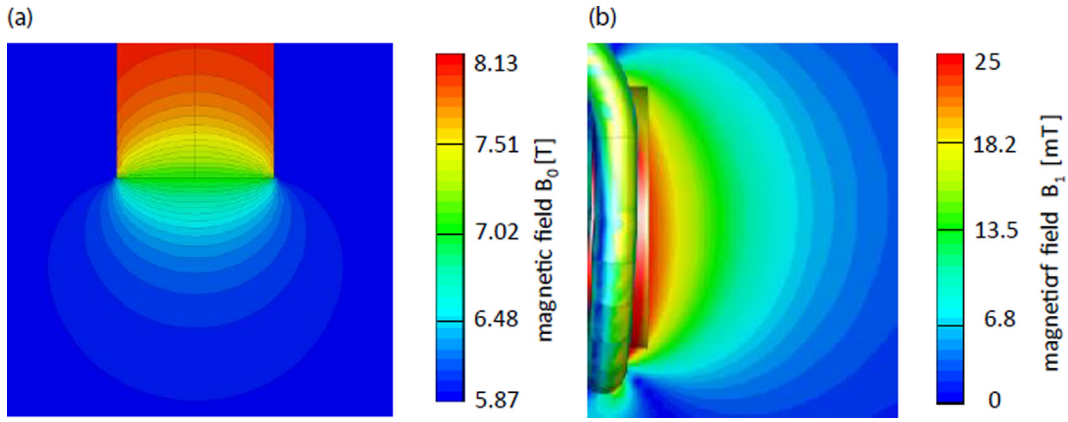

Fig. 7. (a) Simulation of the magnetic field of a ferromagnetic cylinder with radius $R \sim 100$ µm, length $L \sim 3$ mm and $B_{sat} = 2.3$ T in the external magnetic field B_{ext}. (b) Simulation of the magnetic field produced by the microcoils along the x-dimension and the y-dimension, respectively. The following parameters were used: diameter of the coils 150 µm, length 180 µm, the number of windings 6, current 1.34 A for the x-coil and 0.45 A for the y-coil. The color bar is shown for the x-coil. For the y-coil, the magnitude of the magnetic field is proportional to the current.

environment from earlier work. Furthermore, this implementation aims to reduce the line inductance and unintentional coupling of rf-radiation to the coils/cantilever. The heat sink capabilities could be further improved by inducing thermal interface material between the coil windings and the glass chip.

As a sample we used a single crystal $(NH_4)_2SO_4$ cut to the letters "ETH" by focused ion beam milling technique (FIB). The sample was glued to the tip of a commercially available cantilever (quality factor $Q \approx 3000$, spring constant $k \approx 2.5\ \frac{mN}{m}$ and resonance frequency $f_c \approx 1037$ Hz).

3.2. Acquisition and image reconstruction

The 3D image was recorded by measuring 80, 35 and 16 image points in the x-, y- and z-dimension. In total 6 averages were recorded per data point which resulted in a total measurement time, with a delay between scans of 8 s requested by the long relaxation time of the sample, of about 29 days. In the x-dimension, the frequency-encoding was done by a nutation experiment while increasing the nutation time from 0.04 µs to 39.5 µs in steps of 0.5 µs which results in 80 image points. Measured nutation frequencies in the x-dimension ranged from 520 kHz to 950 kHz. In the y-dimension, the Frequency-encoding was done in the same way by increasing the nutation time from 0.04 µs to 51 µs in steps of 1.5 µs. The nutation frequencies ranged from 115 kHz to 300 kHz. During the cyclic adiabatic inversion pulses of the detection period the mean rf amplitude over the whole sample was 45 kHz.

For the reconstruction of the x- and y-dimension the measured nutation curves were zero-filled to twice as many data points and Fourier-transformed. This leads to a spatial distribution of nutation frequencies along the corresponding dimension. To calculate a spatial-axis from the nutation-axis, Eq. (2) for the field $B_{1,x}$ (resp. $B_{2,y}$) was used. Since the $B_{1/2,x/y}$ field gradients are not uniform, the voxel and the spatial resolution increase for longer distances from the coil. Therefore, the signal intensities were weighted with respect to the voxel size to correctly represent the proton density of the sample.

Two Hadamard-8 blocks were used to spatially resolve the z-dimension [17]. One Hadamard block had a width of 430 kHz which leads to a width of 54 kHz of a single resonance slice. To calculate a spatial coordinate from the Larmor frequency, Eq. (1) was used. Even though the voxel size increases for longer distances from the gradient source, the signal intensity has not to be weighted with respect to the voxel size for an accurate representation of the spin density. This is caused by a cancellation of the signal-enhancement at stronger gradient with the decreased width of the resonance slice. The reason is that less spins in spatially narrower resonance slices are measured with a stronger field gradient and therefore sensitivity when keeping the frequency width of the resonance slice constant.

The stability of the setup over the total measurement time is an important criterium for generating well-resolved 3D images. Drifts of the cylindrical gradient source over days is an occurring phenomenon in our setup (in the range of several micrometers). To minimize the distortions of the 3D image by such drifts we tracked the position of the gradient by the spy-cam located inside the probe and made control measurements. If necessary the position of the gradient was corrected as the gradient's position can be controlled from outside the enclosed setup by piezo-engines in x-, y- and z-dimension.

4. Discussion

The presented 3D image is resolved with a mean voxel size of about 5 μm^3 which is a significant improvement compared to inductively detected (micro-) MRI by a factor 5–8 [1,22]. The features of the ETH-sample are partially visible and the missing lower part of "E" shows the limit of the sample dimensions for this type of imaging. The resolution of the image was estimated to be slightly larger than the voxel size and corresponds to about 10 μm^3.

Long measurement times and therefore instabilities/drifts of the setup with a corresponding reduction in resolution could be decreased by doping the material with paramagnetic impurities to shorten the T_1-relaxation time and therefore the recycle delay. Most susceptible for drifts is the position of the ferromagnetic gradient source. Moving it accurately back over the sample after Fourier-encoding could be improved by a more stable voltage control of the piezo bender. Furthermore for solid samples, lowering the temperature of the setup would decrease thermal drifts.

Several improvements that would lead to smaller voxel sizes can be imagined. In this work we used a commercially available cantilever for detection. Using specialized cantilevers according to our needs, the quality factor Q could be increased from 3000 (in our experiment) to several 10,000 [23,24]. This would increase the sensitivity of our experiment and smaller samples and voxels could be measured. Placing the ferromagnetic gradient source closer to the sample would further increase the gradient strength at the sample's position along the z-dimension. Optimizing the

gradient size with respect to the sample size could further increase the gradient strength and therefore the resolution along the z-dimension. Note that by decreasing the gradient size, the accurate re-positioning of the gradient after flipping it back gets more critical. Sending more current through the microcoils would increase the gradient strength along the x- and y-dimension. Especially the y-coil would support much more current than used in our experiment. Furthermore, performing line narrowing experiments (i.e., homonuclear decoupling by magic-echo pulse sequence) could lead to further increase in resolution [25,26].

The total measurement time of our experiment is given by the number of data points and the waiting-time between two measurements. This waiting time depends on the T_1-relaxation of the sample's material (about 4.5 s in our case) and was set to 8 s. This leads to a total measurement time of about 29 days with an SNR of 6–8. Microscale imaging by inductively detected NMR reported for example by Weiger et al. [1] and Chen et al. [4] showed a SNR (43 and 200, respectively) while the measurement time was around 55 h with a considerably larger voxel size (27 and 22 μm^3). Shortening the T_1-relaxation time in our sample (to about 400 ms), our measurement would be decreased to about 43 h. Taking the higher external magnetic fields (factor 1.6 to 3.2) and the decreased temperature for the reported inductively detected measurements into account, one ends up with an SNR in the same order of magnitude for the same measurement time for force-detected and inductively detected NMR but with a 5 times smaller voxel volume. If one is interested in only a certain part of the sample (here a single resonance slice) would decrease the measurement time to 43 h.

5. Conclusion

We described the extension of the 2D imaging by Hadamard- and Fourier-encoding by MRFM to 3D imaging using wire-bonded microcoils for the x- and y-dimension. We used a voxel size of about 5 μm^3. The actual resolution is slightly lower and corresponds to a voxel size of 10 μm^3. This would already allow subcellular imaging of biological cells that could be combined with information such as T_1 and T_2 relaxation times, chemical shifts and diffusion coefficients of different compartments. Further improvement of our setup could lead to a resolution of a few 100 nm in each dimension and allow for interesting applications in biology and material science (i.e., single biological cells, polymer science).

Acknowledgments

This work was supported by the Swiss National Science Foundation (Grant 200020_159707 and 200020_178792). We thank Dr. Luiz Grafulha Morales from ScopeM for preparing the sample by focused ion beam milling.

Appendix A. Supplementary material

Supplementary data associated with this article can be found, in the online version, at https://doi.org/10.1016/j.jmr.2019.01.005.

References

[1] M. Weiger, D. Schmidig, S. Denoth, C. Massin, F. Vincent, M. Schenkel, M. Fey, NMR microscopy with isotropic resolution of 3 μm using dedicated hardware and optimized methods, Concepts Magn. Reson. Part B: Magn. Reson. Eng. 33B (2008) 84–93.
[2] E. Moore, R. Tycko, Micron-scale magnetic resonance imaging of both liquids and solids, J. Magn. Reson. 260 (2015) 1–9.
[3] D.E. Demco, B. Blümich, Solid-state NMR imaging methods. Part II: Line narrowing, Concepts Magn. Reson. 12 (2000) 269–288.
[4] H.-Y. Chen, R. Tycko, Low-temperature magnetic resonance imaging with 2.8 μm isotropic resolution, J. Magn. Reson. 287 (2018) 47–55.
[5] J.A. Sidles, Noninductive detection of single-proton magnetic-resonance, Appl. Phys. Lett. 58 (1991) 2854–2856.
[6] J.A. Sidles, Folded Stern-Gerlach experiment as a means for detecting nuclear magnetic resonance in individual nuclei, Phys. Rev. Lett. 68 (1992) 1124–1127.
[7] J.A. Sidles, J.L. Garbini, K.J. Bruland, D. Rugar, O. Züger, S. Hoen, C.S. Yannoni, Magnetic resonance force microscopy, Rev. Mod. Phys. 67 (1) (1995) 249.
[8] D. Rugar, O. Zuger, S. Hoen, C.S. Yannoni, H.M. Vieth, R.D. Kendrick, Force detection of nuclear magnetic resonance, Science 264 (1994) 1560–1563.
[9] N. Nestle, A. Schaff, W.S. Veeman, Mechanically detected NMR, an evaluation of the applicability for chemical investigations, Prog. Nucl. Magn. Reson. Spectrosc. 38 (2001) 1–35.
[10] J.A. Sidles, D. Rugar, Signal-to-noise ratios in inductive and mechanical detection of magnetic resonance, Phys. Rev. Lett. 70 (22) (1993) 3506–3509.
[11] C.L. Degen, M. Poggio, H.J. Mamin, C.T. Rettner, D. Rugar, Nanoscale magnetic resonance imaging, Proc. Natl. Acad. Sci. U. S. A. 106 (2009) 1313–1317.
[12] O. Zuger, S.T. Hoen, C.S. Yannoni, D. Rugar, Three-dimensional imaging with a nuclear magnetic resonance force microscope, J. Appl. Phys. 79 (1996) 1881–1884.
[13] S.-H. Chao, W.M. Dougherty, J.L. Garbini, J.A. Sidles, Nanometer-scale magnetic resonance imaging, Rev. Sci. Instrum. 75 (2004) 1175–1181.
[14] S. Tsuji, T. Masumizu, Y. Yoshinari, Magnetic resonance imaging of isolated single liposome by magnetic resonance force microscopy, J. Magn. Reson. 167 (2004) 211–220.
[15] H.J. Mamin, M. Poggio, C.L. Degen, D. Rugar, Nuclear magnetic resonance imaging with 90-nm resolution, Nat. Nanotechnol. 2 (2007) 301–306.
[16] K.W. Eberhardt, A. Hunkeler, U. Meier, J. Tharian, S. Mouaziz, G. Boero, J. Brugger, B.H. Meier, Two-dimensional magnetic resonance force microscopy using full-volume Fourier and Hadamard encoding, Phys. Rev. B 78 (2008).
[17] K.W. Eberhardt, C.L. Degen, B.H. Meier, Fast magnetic resonance force microscopy with Hadamard Encoding, Phys. Rev. B 76 (2007) 180405.
[18] A.W. Jones, J. BlandHawthron, P.L. Shopbell, Towards a general definition for spectroscopic resolution, Astr. Soc. P 77 (1995) 503–506.
[19] C. L. Degen. Magnetic resonance force microscopy: NMR spectroscopy on the micro- and nanoscale. ETH Zürich, Diss. No. 17562, 2008.
[20] Q. Lin. Magnetic resonance and magnetic double resonance in force detection: Design and application. ETH Zürich, Diss. No. 16706, 2006.
[21] A. Schaff, W.S. Veeman, Mechanically detected nuclear magnetic resonance at room temperature and normal pressure, J. Magn. Reson. 126 (1997) 200–206.
[22] L. Ciobanu, D.A. Seeber, C.H. Pennington, 3D MR microscopy with resolution 3.7 μm by 3.3 μm by 3.3 μm, J. Magn. Reson. 158 (1–2) (2002) 178–182.
[23] S. Mouaziz, G. Boero, G. Moresi, C.L. Degen, Q. Lin, B.H. Meier, J. Brugger, Combined Al-protected and HF-vapor release process for ultrathin single crystal silicon cantilevers, Microelectron. Eng. 83 (2006) 1306–1308.
[24] Y. Tao, C.L. Degen, Facile fabrication of single-crystal-diamond nanostructures with ultrahigh aspect ratio, Adv. Mater. 25 (2013) 29.
[25] G.S. Boutis, P. Cappellaro, H. Cho, C. Ramanathan, D.G. Cory, Pulse error compensating symmetric magic-echo trains, J. Magn. Reson. 161 (2003) 132–137.
[26] C.L. Degen, Q. Lin, B.H. Meier, Dipolar spin echos in magnetic resonance force microscopy, Phys. Rev. B 74 (2006) 104414.